

Programming an Enhanced Uptake and the Intracellular Fate of Magnetic Microbeads

Ecem Tiryaki, Saida Ortolano, Gustavo Bodelón, and Verónica Salgueiriño**

This study compares two kinds of magnetic microbeads with different surface features and cell entry pathways, aiming to provide insights into how to program their cell uptake and intracellular fate. It is found that a rougher surface enhances the cell uptake of the microbeads, regardless of whether they are pulled by a magnetic field gradient or adsorbed by the cell membrane. However, the entry route affects the intracellular localization of the microbeads: The magnetically dragged microbeads reach the cytoplasm, while the adsorbed microbeads stay in the late endosomes and lysosomes. This suggests that different strategies can be used to target different cellular compartments with magnetic microbeads. Moreover, it is demonstrated that the cells containing the microbeads can be moved and regrown at specific locations by applying a magnetic field gradient, showing the potential of these magnetic microbeads for cell delivery and manipulation.

drug delivery,^[5] and imaging,^[6] considering their superparamagnetism, high chemical stability attributed to their low propensity for further oxidation, and low toxicity.^[7] However, the main challenge is the unpredictable or uncontrolled functional response of the magnetic material in complex biological systems.^[8,9] Therefore, different strategies have been studied, considering the main physicochemical parameters (chemical composition, size, shape, surface charge, surface area, surface coating, and biotransformation) that affect the interactions between particles and living organisms, highlighting surface topography as a key factor in the cellular response.^[10]

Nanoscale topographical features such as pores, ridges, and fibers lie within the same order of magnitude of cell receptors and membrane and intracellular proteins,

and can therefore trigger biophysical signals influencing cell processes, such as cell adhesion, morphology, migration, proliferation, and gene expression.^[11,12] By engineering artificial microenvironments with nanoscale topographical features in different surface patterns and structures, it is possible to investigate cell behavior and diverse cellular processes such as endocytosis. Some of the methods used to create nanotopographical surfaces include scaffolds,^[13,14] hydrogels,^[15] and patterned nanostructured surfaces.^[16,17] For instance, nanopillar quartz substrates were shown to influence the curvature in the plasma membrane so as to enhance the endocytosis of integrin receptors, leading to the disassembly of focal adhesions and stress fibers.^[18] Hence, the nanoscale surface topography has become a central topic when designing new strategies to enhance the internalization and therapeutic outcome of nano and microparticles,^[19] with particular interest in the role played by anisotropic, elongated, or with high aspect ratio nanostructures.^[20–22]

Inspired by these research results, herein we investigated how the nanoscale surface topography influences the internalization, intracellular fate, and cytotoxicity of magnetic microbeads with polystyrene (PS) cores but different iron oxide-based nanostructured shells, bearing therefore distinct surface topographies. In addition, we compared two ways of delivering the microbeads into the cells: magnetic actuation and adsorptive uptake. The former uses a magnetic field gradient to overcome the endolysosomal pathway that occurs for the latter, allowing both types of microbeads to reach the cytoplasm directly. Remarkably, in both routes, the rougher nanoscale topography of the microbeads favors the cell uptake, even when guided by the magnetic field

1. Introduction


Magnetic nanoparticles and microbeads are widely used in biomedicine,^[1] especially for cell therapy,^[2] hyperthermia,^[3,4]

E. Tiryaki, G. Bodelón, V. Salgueiriño
CINBIO
Universidade de Vigo
Vigo 36310, Spain
E-mail: gbodelon@uvigo.es; vsalgue@uvigo.es

S. Ortolano
Rare Diseases and Pediatric Medicine Research Group
Galicia Sur Health Research Institute (IIS Galicia Sur)
SERGAS-UVIGO
Hospital Álvaro Cunqueiro
Vigo 36312, Spain

G. Bodelón
Departamento de Biología Funcional y Ciencias de la Salud
Universidade de Vigo
Vigo 36310, Spain

V. Salgueiriño
Departamento de Física Aplicada
Universidade de Vigo
Vigo 36310, Spain

 The ORCID identification number(s) for the author(s) of this article can be found under <https://doi.org/10.1002/adhm.202301415>

© 2023 The Authors. Advanced Healthcare Materials published by Wiley-VCH GmbH. This is an open access article under the terms of the Creative Commons Attribution-NonCommercial License, which permits use, distribution and reproduction in any medium, provided the original work is properly cited and is not used for commercial purposes.

DOI: 10.1002/adhm.202301415

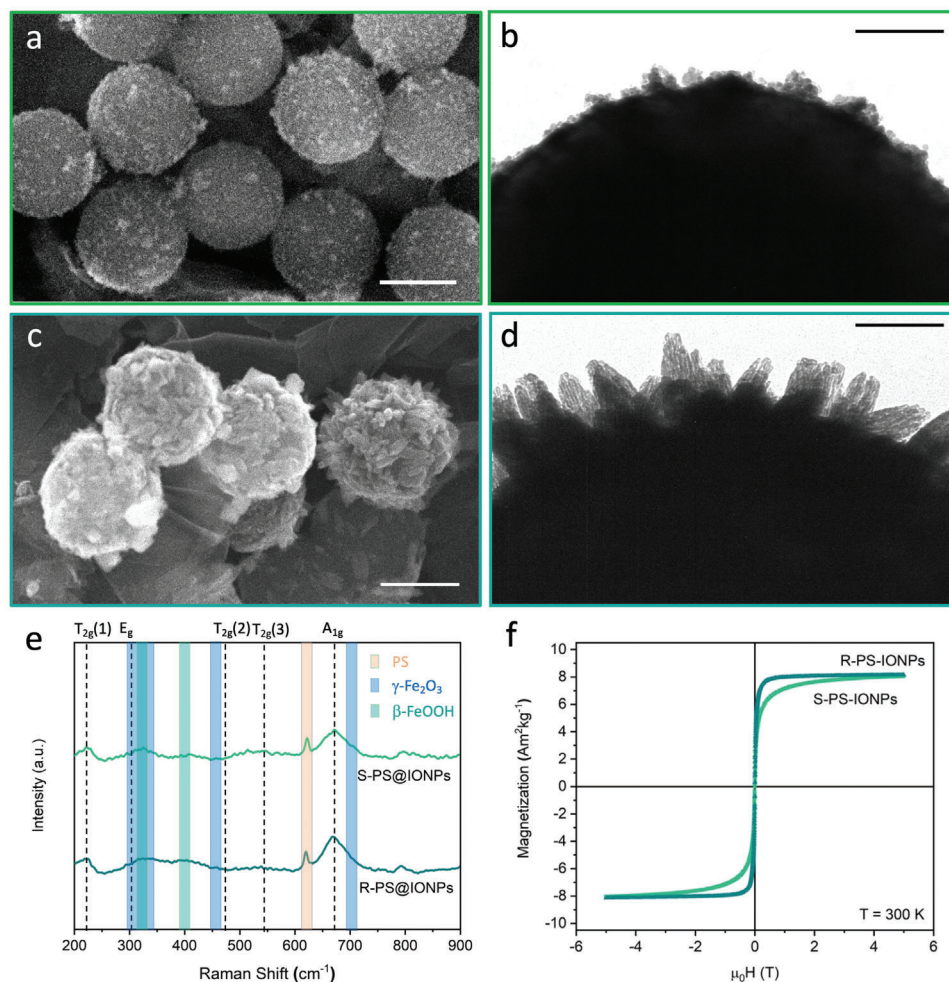


Figure 1. a,c) SEM (scale bar: 1 μm) and b,d) TEM (scale bar: 200 nm) images, e) Raman spectra and f) field-dependent magnetization at room temperature, of the microbeads with smoother (S-PS@IONPs) or rougher (R-PS@IONPs) surface topology, respectively.

gradient and despite showing similar values of saturation magnetization. As a proof-of-concept application, the two types of microbeads were shown to efficiently allow the spatial manipulation of the cells that have internalized them, under the action of a magnetic field gradient, achieving good levels of cell viability. Our work paves the way for strategies that take advantage of adjustable nanoscale features on the surface of core-shell magnetic microbeads, holding great potential for biomedical applications and, in particular, for cell therapy.

2. Results and Discussion

2.1. Core@shell PS@IONPs Nanostructured Microbeads

To investigate the effect of the nanoscale surface topography of microbeads on their interaction with living cells, iron oxide nanoparticles (IONPs) with different shape and magnetic phase (spherical ($\text{Fe}_3\text{O}_4/\gamma\text{-Fe}_2\text{O}_3$) or elongated ($\text{Fe}_3\text{O}_4/\beta\text{-FeOOH}$)) were placed on PS spherical templates, to generate a smoother (S) or rougher (R) surface topography, while adding the magnetic functionality. For that, in the first case, presynthesized IONPs

were deposited onto the PS spheres using the LbL self-assembly technique,^[23] offering spherical microbeads with a relatively smooth surface topography (S-PS@IONPs). For the second case, the PS beads were used as substrates on which elongated akaganeite ($\beta\text{-FeOOH}$) nanoparticles were first grown and then partially reduced offering a mixed magnetic phase ($\text{Fe}_3\text{O}_4/\beta\text{-FeOOH}$), such that spiky microbeads with a rougher surface topography (R-PS@IONPs) were produced. **Figure 1** includes representative scanning electron microscopy (SEM) and transmission electron microscopy (TEM) images reflecting the attained morphology and surface topography of the two types of microbeads under consideration. Figure S1 (Supporting Information) shows a TEM general overview, the average size distribution (11.1*/1.0 nm, log-normal fit), the Raman spectra (before and after fixing tetramethyl ammonium hydroxide [TMAOH]^[24] on their surface), and the magnetic characterization of the IONPs deposited onto PS spheres for the production of the S-PS@IONPs microbeads. Both Raman spectra included in Figure S1c (Supporting Information) show the presence of the intense A_{1g} band at 671 cm^{-1} and two less intense, at 300 and 530 cm^{-1} , associated with Fe_3O_4 (areas shaded in

dark blue). The shoulder at 700 cm^{-1} and two subtle bands at 300 and 460 cm^{-1} (areas shaded in light blue) which become more intense after fixing the TMAOH molecules confirm the presence of maghemite ($\gamma\text{-Fe}_2\text{O}_3$) as a second phase. Both the temperature- and field-dependent magnetization plots (Figure S1d–f, Supporting Information) reflect the superparamagnetic behavior of these magnetic nanoparticles synthesized using the Massart method,^[25] with no coercivity at room temperature, a T_B blocking temperature at 215 K and a considerably large value of saturation magnetization. For the deposition of these IONPs, the surface of the PS beads was first prepared using two layers of polyelectrolyte (PAH/PSS), such that it becomes negatively charged and ensures the homogeneous adhesion of the positively charged TMAOH-functionalized nanoparticles. SEM and TEM images in Figure 1a,b confirm that these $\text{Fe}_3\text{O}_4/\gamma\text{-Fe}_2\text{O}_3$ nanoparticles are homogeneously distributed on the PS beads, such that a relatively smooth surface topography was attained.

For the second type of microbeads (R-PS@IONPs), a diffusion-controlled mechanism to induce the growth of elongated iron oxyhydroxide nanoparticles on PS templates was used. The nucleation and growth stages occur via the formation of $[\text{Fe}(\text{H}_2\text{O})_6]^{+3}$ complexes, which become adsorbed on the negatively charged surface of the PS beads and undergo hydrolysis reactions under acidic conditions. These chemical processes imply the formation of $\beta\text{-FeOOH}$ nuclei that grow in a particular direction, offering elongated nanostructures on the surface of the PS spheres.^[26,27] Subsequently, an akaganeite-magnetite topotactical transition was induced using N_2H_4 as a reducing reagent,^[28] and hinted by the change in color observed in the solution, from orange to black. Accordingly, magnetic microbeads of PS spheres coated with elongated IONPs and therefore offering a rougher surface topography (R-PS@IONPs) were produced. Figure 1c,d include SEM and TEM images of the microbeads, revealing this rougher surface due to the elongated IONPs pointing outwards in these microstructures.

To confirm the magnetic phases of the IONPs in both types of microbeads, Raman spectroscopy was used (Figure 1e).^[29] The spectra show two intense bands that can be associated to Fe_3O_4 (the five modes of this iron oxide phase with a spinel structure are indicated with black dotted vertical lines): the very intense A_{1g} band at 671 cm^{-1} and the $T_{2g}(1)$, less intense, at 220 cm^{-1} . If attending now to the spectrum of the S-PS@IONPs microbeads, we can observe it also shows three main bands (around 310 , at 460 , and at 700 cm^{-1}) associated with the presence of maghemite ($\gamma\text{-Fe}_2\text{O}_3$) (shaded in blue). In the case of the R-PS@IONPs microbeads, the spectrum shows the presence of two additional bands located at 325 and 400 cm^{-1} that can be associated with $\beta\text{-FeOOH}$ (areas shaded in green), besides the two already mentioned, much more intense, the A_{1g} band at 671 cm^{-1} and the $T_{2g}(1)$ band at 220 cm^{-1} , which confirm the partial crystalline crossover of the initial oxyhydroxide to magnetite (Fe_3O_4). Other bands with less intensity in both spectra can be associated to the presence of the PS (area shaded in pink) and other iron oxide secondary phases. To further confirm the presence of these magnetic phases and the magnetic behavior associated, vibrating sample magnetometry (VSM) measurements were performed. Figure 1f and Figure S2 (Supporting Information) include the field-dependent magnetization of the two types of microbeads. Figure 1f shows the field-dependent magnetization at room tem-

perature, with hysteresis loops showing no coercivity. The relatively low values of saturation magnetization at 300 K (8.05 and $8.14\text{ A m}^2\text{ kg}^{-1}$ for the S-PS@IONPs and R-PS@IONPs microbeads, respectively) can be justified in terms of the percentage of ferrimagnetic material in the final microbeads, relative to the diamagnetic polymer.^[30] Figure S2 (Supporting Information) compares the hysteresis loops at 10 and 300 K and at low field, such that small values of coercivity at very low temperature (<5 and 25 mT , respectively) can be appreciated. These coercivities can be explained taking into account the superparamagnetic behavior of the magnetic nanoparticles with small crystalline domains, in the final microbeads.^[31]

The microbeads were additionally labeled with an outer layer of PAH-FITC [poly(fluorescein isothiocyanate allylamine hydrochloride)] dye, to render them positively charged to favor attractive electrostatic interactions with the negatively charged cell membrane,^[32,33] and easy to track using confocal fluorescence microscopy. Figure S3a (Supporting Information) shows the initial values of surface ζ -potential of the S-PS@IONPs and R-PS@IONPs microbeads dispersed in pure water ($+40.57$ and $+43.93\text{ mV}$, respectively) and the values attained when dispersing them in two culture media bearing low (OptiMEM; $+9.35$ and $+9.22\text{ mV}$, respectively) and high (DMEM+FBS; -7.20 and -8.12 mV , respectively) concentration of serum proteins. The decrease in surface charge (and even change in sign) observed can be attributed to the increased adsorption of these serum proteins on the microbeads surface, proving their electrostatic stability in the different media. However, given the positive values of ζ -potential attained in DMEM, this medium was not further considered in our investigations. The fluorescence of the microbeads was evaluated by fluorescence spectroscopy (Figure S3b, Supporting Information) and microscopy [S-PS@IONPs (Figure S3c,d, Supporting Information) and R-PS@IONPs (Figure S3e,f, Supporting Information)], proving the successful functionalization with the fluorescent dye.

2.2. Cell Uptake and Intracellular Fate

The influence of the surface topography of the S-PS@IONPs and R-PS@IONPs microbeads in the cell entry and intracellular fate was examined in the human epidermoid carcinoma cell line A431, previously used as an in vitro model to investigate the interaction of tumor cells with magnetic nanoparticles.^[34–36] First, we assessed their internalization applying a static magnetic field gradient. To this end, the microbeads were dispersed in the OptiMEM medium and subsequently, the cells were incubated with each sample of microbeads, independently and for 15 min , to allow their physical interaction with the cellular surface while exposing the cultures to the magnetic field gradient ($\mu_0 H_{\text{max}} = B_{\text{max}} = 15\text{ mT}$, $\text{dB}/\text{dx} = 63\text{ mT m}^{-1}$), which implies a magnetic force to drag the microbeads (a brief analysis is included in the Supporting Information). The unbound microbeads were removed by several washes. Subsequently, the A431 cells were fixed with formalin and the CD44 cell surface protein was immunostained with mouse-anti-human-CD44 and goat anti-mouse antibodies conjugated with Alexa 647, to visualize the plasma membrane and use it as reference of cell boundaries.^[37] Next, the cellular internalization of each type of

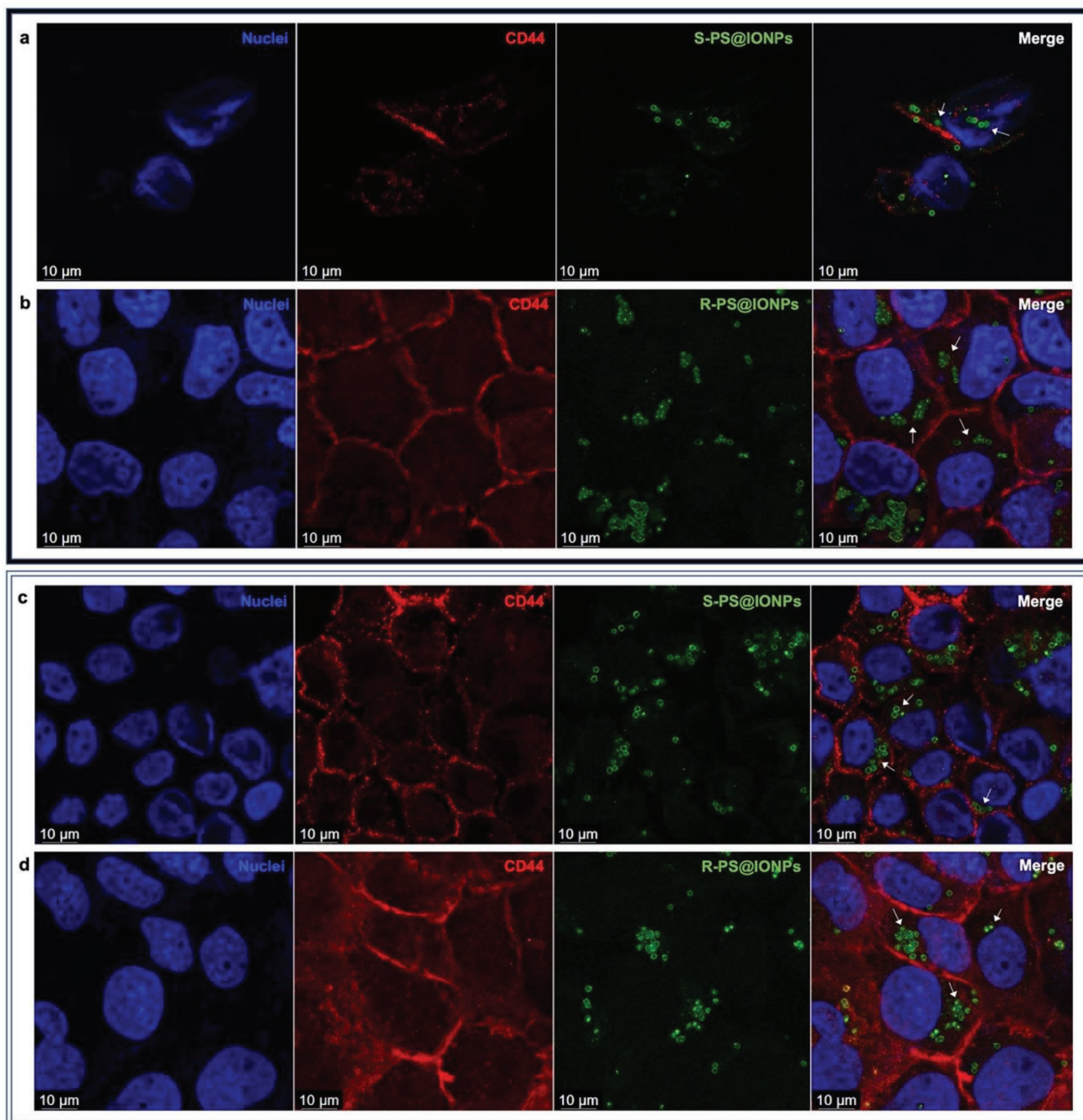


Figure 2. Confocal microscopy analysis of the a,c) S-PS@IONPs and the b,d) R-PS@IONPs internalization in A431 cells under the exposure to a magnetic field gradient (top panel) and by adsorptive uptake (bottom panel), showing: DAPI labeling of cell nuclei (first column; blue), CD44 staining with mouse-anti-human-CD44 antibodies and goat anti-mouse-IgG antibodies conjugated to Alexa Fluor 647 (second column; red), the FITC-labeled microbeads (third column; green), and the merged images (fourth column). The white arrows indicate some of the internalized microbeads.

microbeads was studied by confocal fluorescence microscopy. The cross-sectional images included in the top panel in **Figure 2** show the presence of S-PS@IONPs (Figure 2a, third and fourth column, in green) and R-PS@IONPs (Figure 2b, third and fourth column, in green) that were internalized by magnetic actuation. Analogously, we investigated the internalization of the microbeads in the cell through adsorptive mechanisms in

the absence of magnetic actuation. To this end, the two types of microbeads were incubated separately with A431 cells for 16 h. Afterward, unbound ones were removed, and the cells were fixed and labeled as indicated above. The cross-sectional images included in the bottom panel in **Figure 2** show the presence of S-PS@IONPs (Figure 2c, third and fourth column, in green) and R-PS@IONPs (Figure 2d, third and fourth column, in green)

that were internalized by adsorptive uptake. Additional confocal microscopy images further demonstrating the internalization of both types of microbeads, with and without the magnetic actuation, are shown in Figure S4 (Supporting Information). Altogether, these data demonstrate that S-PS@IONPs and R-PS@IONPs access the intracellular milieu by both magnetic actuation and adsorptive uptake.

To shed light on a potentially different intracellular fate of these microstructures upon magnetic actuation or adsorptive uptake, we assessed their localization inside endosomes and lysosomes. Endosomes are dynamic subcellular structures that undergo fusion and fission events to yield late endosomes, and eventually lysosomes.^[38] This process is finely controlled by the sequential recruitment of various endosomal proteins such as Rab7, a GTPase involved in the aggregation and fusion of late endosomes and lysosomes,^[39] and commonly used as a bona fide marker of late endosomes/endolysosomes.^[40] Accordingly, we used it to evaluate the localization of the two types of microbeads, and to this end, the cells were fixed with formalin, permeabilized with PBS 0.1% triton X-100, and subsequently immunostained with rabbit anti-human-Rab7 and Alexa 594-goat anti-rabbit-IgG antibodies. The immunolabeling of CD44 was performed simultaneously with Rab7 and control experiments demonstrated the specificity of the Rab7 immunostaining (see third column in Figure S5, Supporting Information). Taking these control experiments as reference, the confocal microscopy images included in the top panel in **Figure 3** show that neither S-PS@IONPs (Figure 3a, fourth column) nor R-PS@IONPs (Figure 3b, fourth column) colocalize with Rab 7-labeled endosomal compartments, implying that the internalization of the microbeads by magnetic actuation bypasses the endosomal uptake. Unequally, when the internalization into the cells was promoted by adsorptive uptake, both types of PS@IONPs microbeads colocalize with Rab7 protein, as shown in the bottom panel in Figure 3. The insets in the merged images in the fourth column of this bottom panel show regions of colocalization between the Rab7-labeled endosomes and S-PS@IONPs (Figure 3c), as well as in the case of R-PS@IONPs microbeads (Figure 3d). The reader should ponder the fact that the colocalization of Rab7 (yellow) and the FITC-labeled microbeads (green) yields red-orange-colored areas in the confocal microscope images. These results indicate that in the absence of the magnetic field gradient both types of PS@IONPs microbeads localized in the late endosomes. The images also show that not all the internalized microbeads colocalize with the endosomal marker, suggesting that they do not enter the cells simultaneously. Additional confocal microscopy images confirming these observations related to the colocalization of the microbeads after proceeding with the two internalization strategies are shown in Figure S6 (Supporting Information).

These findings encouraged the assessment of a potential colocalization of the internalized microbeads with lysosomes.^[41] For this purpose, control experiments demonstrating the effective staining of the lysosomes organelles with the LysoTrackerRed DND-99 fluorescent dye were performed and are shown in Figure S7 (Supporting Information). Considering the internalization of the microbeads, the confocal microscopy images shown in **Figure 4** reveal that whereas the magnetic actuation (top panel) does not elicit colocalization of S-PS@IONPs (Figure 4a) and R-PS@IONPs (Figure 4b) with lysosomes, their internaliza-

tion through the endosomal route by means of adsorptive uptake (bottom panel) involves their inclusion within lysosomal compartments in both cases (S-PS@IONPs (Figure 4c) and R-PS@IONPs (Figure 4d)). The insets in these merged images in the bottom panel show zoomed out regions of colocalization of both the microbeads and the lysosomes. The DAPI staining of nuclei and CD44 labeling of the same images are shown in Figure S8 (Supporting Information). These results prove that, as opposed to magnetic actuation, adsorptive uptake of both types of PS@IONPs microbeads by A431 cells takes place through endocytosis, eventually leading to their accumulation in late endosomes and lysosomes.

Similar results showing the localization of superparamagnetic particles dispersed in the cytoplasm if pushed by a magnetic force or trapped in lysosomes if endocytocized, were reported, but employing much smaller alginate-coated magnetic nanoparticles functionalized with folate (95 nm size and -22 mV ζ -potential).^[42] Since size is considered a key parameter in these routes (being the optimal around 50 nm),^[43,44] and given that large particles (>500 nm) are known to be internalized only via phagocytosis and/or micropinocytosis or by membrane-wrapping,^[45,46] we can point these processes for the adsorptive uptake as the most probable, given the rather large size of these microbeads (with an average diameter $d \approx 1.4$ μm), though this issue awaits further investigations. Yet, we have not observed significant differences regarding the interaction of S-PS@IONPs or R-PS@IONPs microbeads with Rab7-labeled endosomes and lysosomal compartments when internalized, which hints at similar intracellular trafficking given the similar surface chemistry. In this regard, IONPs either functionalized with 3-aminopropyltriethoxysilane (122 nm size and $+23$ mV ζ -potential) or with dimercaptosuccinic acid (83 nm size and -34 mV ζ -potential) in RAW264.7 macrophages, were both found to accumulate in Rab7⁺ endolysosomes, despite of proceeding through a different intracellular trafficking kinetics.^[47]

Since the PS@IONPs microbeads differ mainly in terms of their surface topography, we investigated whether this feature would play any role in their endosomal trafficking, because of interacting differently with cellular proteins, upon internalization by adsorptive uptake. With this objective in mind, we evaluated the protein profile associated to each type of microbead, after lysing the A431 cells and recovering the internalized microbeads applying a magnet. The proteins bound to the S-PS@IONPs and R-PS@IONPs microbeads were eluted from the microbead surface by boiling and subsequently analyzed by SDS-PAGE. **Figure 5a** shows the protein profiles obtained from cell lysates of cells not incubated with the microbeads (lane 1, control), and from cells incubated with S-PS@IONPs (lane 2) or with R-PS@IONPs (lane 3) microbeads which were internalized. Though the profiles are very similar, the intensity of the protein bands yielded and associated to the R-PS@IONPs is significantly higher than that of the S-PS@IONPs microbeads. This can be explained considering either a higher amount of R-PS@IONPs microbeads internalized and/or a larger surface area, as compared to S-PS@IONPs. To further investigate these results, we quantified the cellular uptake of microbeads in A431 cells by inductively coupled plasma optical emission spectrometry (ICP-OES). **Figure 5b** plots the percentage of Fe content in the cells, reflecting the higher internalization of the R-PS@IONPs microbeads in the two routes

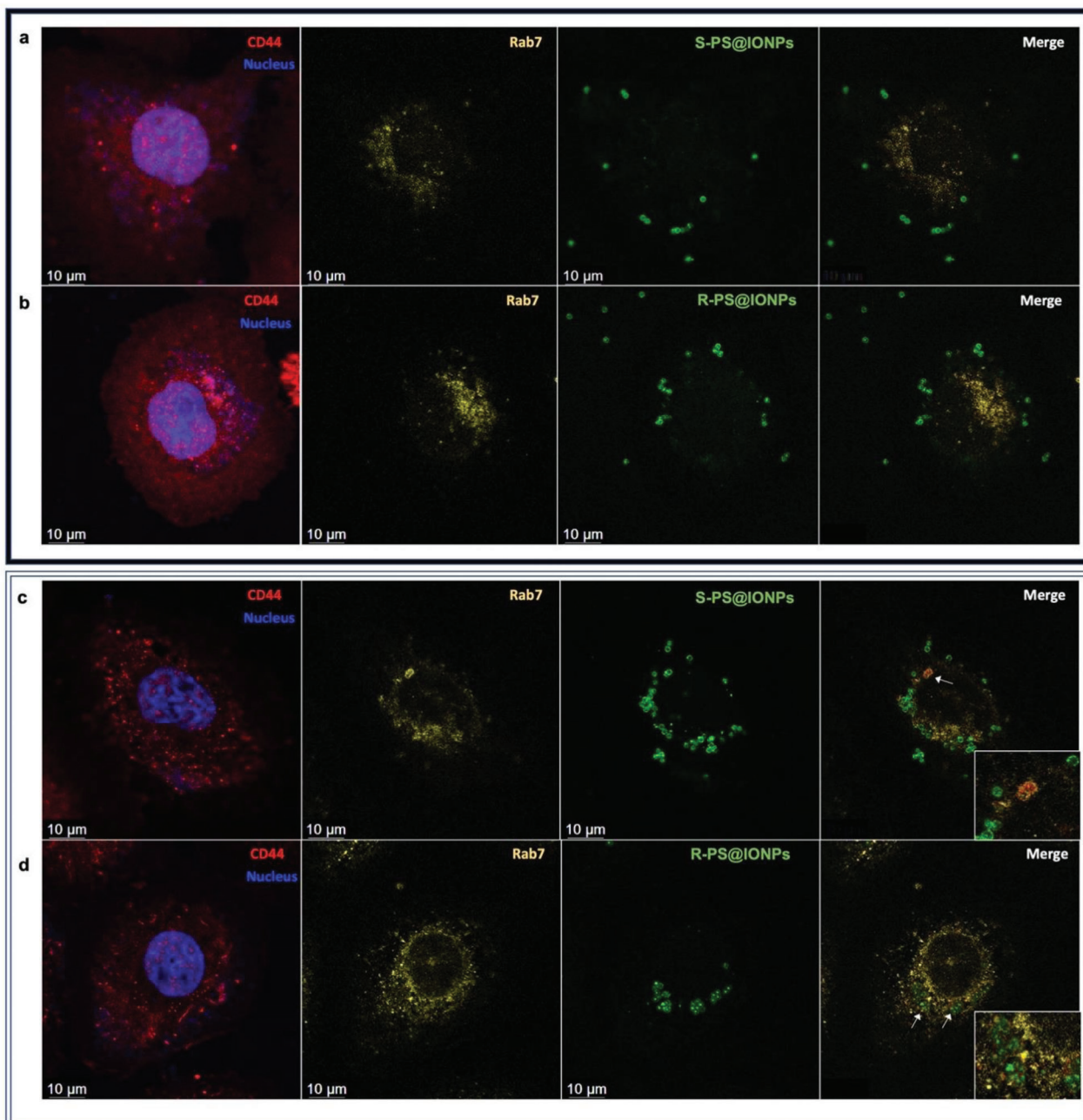


Figure 3. Confocal microscopy images of the a,c) S-PS@IONPs and the b,d) R-PS@IONPs colocalization with Rab7 after internalization in A431 cells due to the exposure to a magnetic field gradient (top panel) and by adsorptive uptake (bottom panel), showing: DAPI labeling of cell nuclei and CD44 staining with mouse-anti-human-CD44 antibodies and goat anti-mouse-IgG antibodies conjugated to Alexa Fluor 647 (first column; blue and red), Rab7 staining with rabbit anti-human-Rab7 antibodies, and goat anti-rabbit-IgG antibodies conjugated to Alexa 594 (second column; yellow), the FITC-labeled microbeads (third column; green) and the merged images (fourth column) showing colocalization regions (indicated with white arrows) of Rab 7 and microbeads.

employed (lighter colors refer to the cellular uptake and the darker colors refer to the magnetic actuation when using both types of microbeads). Certainly, the amount of R-PS@IONPs internalized by adsorptive uptake was almost fourfold higher than S-PS@IONPs, and can therefore be associated to the surface topography, stemming from the elongated IONPs pointing outward. Noticeably, upon exposure to the magnetic field gradient,

the amount of R-PS@IONPs internalized was 1.8-fold higher than S-PS@IONPs, despite the very similar values of saturation magnetization ($8.14 \text{ A m}^2 \text{ kg}^{-1}$ (R-PS@IONPs) versus $8.05 \text{ A m}^2 \text{ kg}^{-1}$ (S-PS@IONPs) at 300 K), which implies a similar total magnetic moment and consequently a comparable force exerted by the magnetic field gradient.^[48] This outcome points again to the increased surface roughness (i.e., surface topography) of the

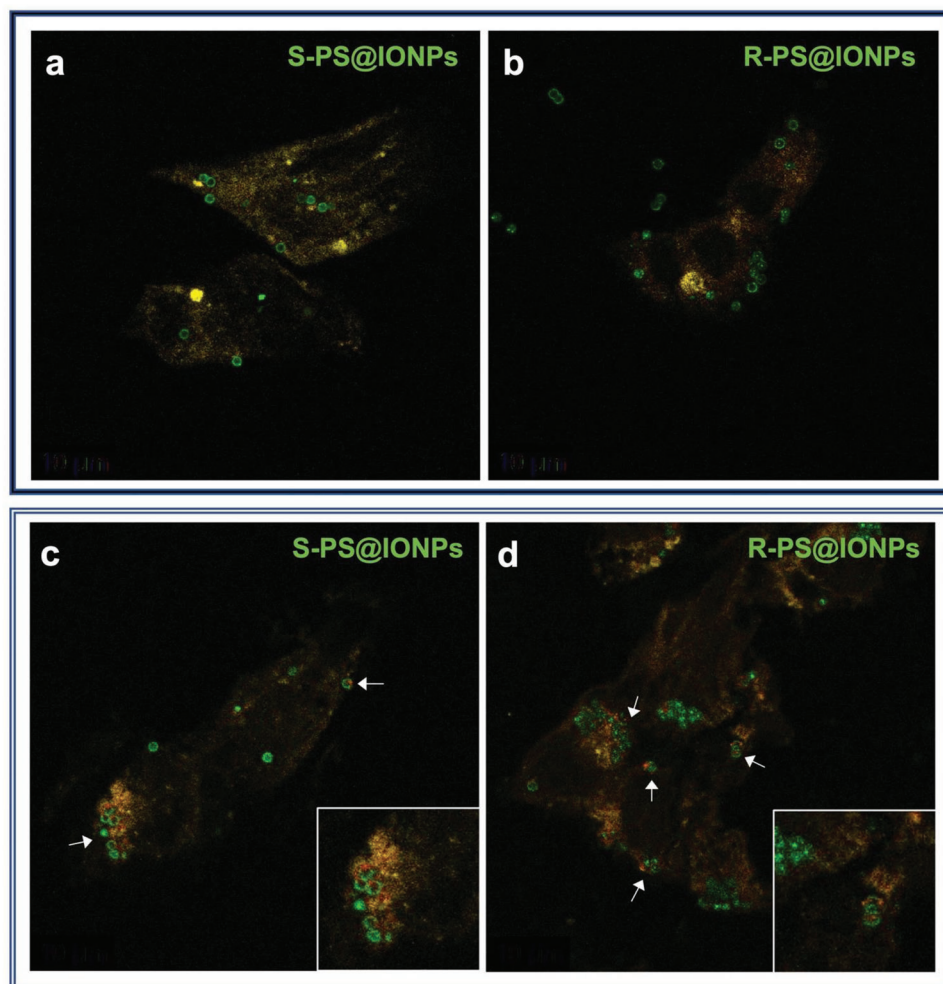


Figure 4. Confocal microscopy analysis of colocalization of the a,c) S-PS@IONPs and the b,d) R-PS@IONPs with lysosomes upon the internalization in A431 cells, under the exposure to a magnetic field gradient (top panel) and by adsorptive uptake (bottom panel), showing the FITC-labeled microbeads (green) and the lysosome staining with LysoTracker (yellow). The insets and white arrows show regions of colocalization of the particles and lysosomal compartments because of the adsorptive uptake.

R-PS@IONPs microbeads, to play a role for the enhanced cellular uptake.

Summarizing this part, the internalization is more effective in the case of the R-PS@IONPs microbeads with the coarser surface topography, both in the absence or presence of the magnetic field gradient. In relation to this, dissipative particle dynamics simulations were adopted to examine the effect of spikes located on the surface of nanoparticles to promote cellular uptake.^[49] To validate how this surface topological structure affects its translocation across the cell membrane, the simulations determined that the nanostructures with spikes on their surface can perturb the bilayer structure once adhered on it, increasing the lateral defects of the bilayer, decreasing the vertical deformation of the bilayer and lowering the density of nearby lipids during the translocation process. This mechanism was demonstrated to depend on a threshold penetration force acting on the particles for the translocation process during the adsorptive uptake, which is exerted both on spherical or spiky nanoparticles but becomes more effective when considering particles with long and sparse spikes.^[49] For

the magnetic actuation, we can hypothesize then a sum of forces, this penetration force acting on the particles as approaching the membrane and the magnetic force exerted by the magnetic field gradient, which can therefore explain the more effective internalization of microbeads. Analyzing the forces separately, we can assume the penetration force to be larger and more effective on the R-PS@IONPs microbeads because of the spikes and the magnetic force to be similar in both types of microbeads, attending to the similar values of saturation magnetization ($\approx 8 \text{ A m}^2 \text{ kg}^{-1}$). Consequently, the percentages of Fe correlating with the amount of microbeads internalized by both routes just prove the critical role of the penetration force stemming from the coarser surface topology in comparison with the magnetic force.

To assess the potential cytotoxicity of both types of PS@IONPs microbeads, cultures of A431 cells were incubated in the same conditions but with different concentrations of microbeads (ranging from 50 to 300 μg per cell culture) before evaluating their metabolic activity (i.e., viability) by MTT assays. This test registers the formation of a purple-colored precipitate that can be

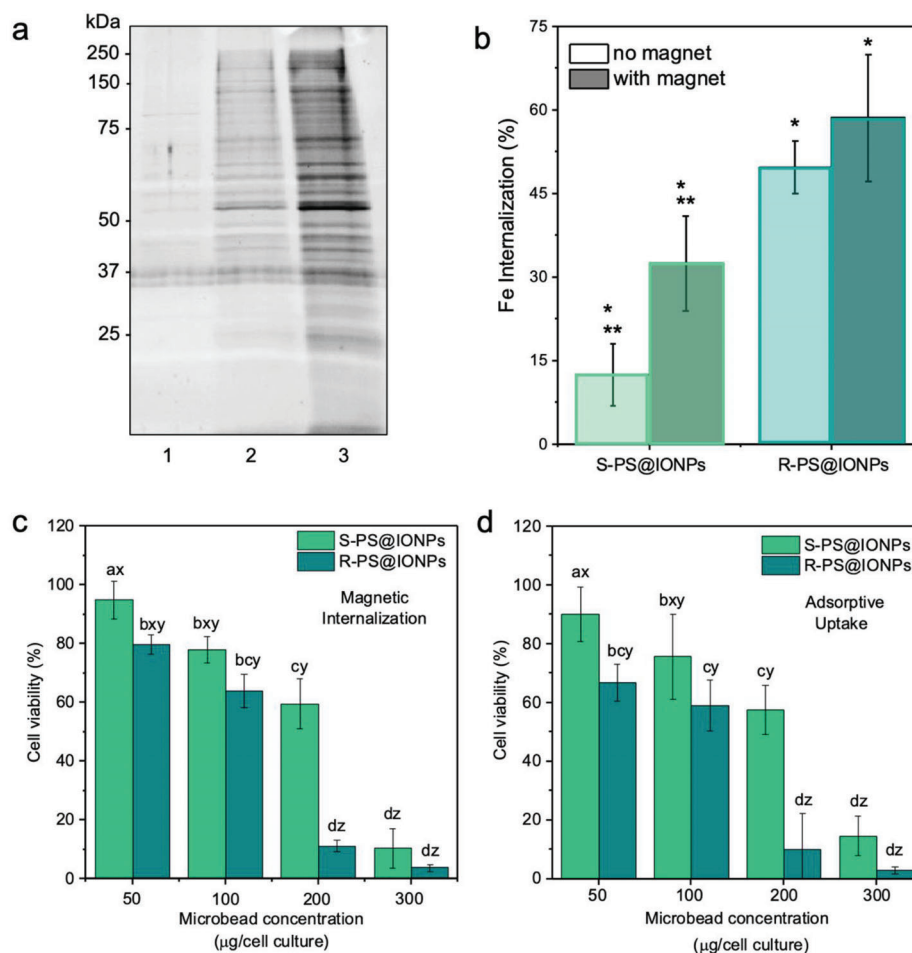


Figure 5. a) SDS-PAGE analysis of the protein profile associated to proteins from cell lysates not incubated with microbeads (lane 1), incubated with S-PS@IONPs (lane 2), and incubated with R-PS@IONPs (lane 3) microbeads, b) percentage of Fe (by ICP-OES analysis) present in cells after the internalization of the microbeads by means of the magnetic actuation (darker bars) or by adsorptive uptake (lighter bars). Each bar corresponds to the mean \pm standard deviation of three replicates. Statistical significance: * $p < 0.05$ compared with values of S-PS@IONPs and R-PS@IONPs, ** $p < 0.05$ compared with values of the magnetic actuation and adsorptive uptake for each sample (independent and paired samples *t*-tests). Viability of the A431 cells exposed to S-PS@IONPs and R-PS@IONPs microbeads considering: c) the magnetic manipulation and d) the adsorptive uptake at the indicated concentrations. Each bar represents the mean \pm standard deviation of three independent tests. Significant differences are indicated by (a)–(d) ($p < 0.05$, Tukey's test) among microbead concentration for each sample and x - z ($p < 0.05$, Tukey's test) between S-PS@IONPs and R-PS@IONPs for each microbead concentration. There is no significant difference between magnetic actuation and adsorptive uptake for each sample.

measured spectrophotometrically if the cells are viable and capable of metabolizing the 3-(4,5-dimethylthiazol-2-yl)-2,5-diphenyl tetrazolium bromide compound. Figure 5c,d shows the percentage of cell viability, which decreases as increasing the microbeads concentration employed, being more remarkable this reduction in the metabolic activity in the case of the R-PS@IONPs microbeads. This higher cytotoxicity associated to the R-PS@IONPs microbeads can in principle be attributed to the larger values of internalization, but a synergistically more toxic effect because of the surface topography cannot be ruled out at this point.

2.3. Magnetic Manipulation

A key application of magnetic nanoparticles in the biomedical field resides in its yet largely unexplored capability to

influence tissues,^[50] cells,^[51] and even cellular functions^[52] by remotely applying a magnetic field gradient. In particular, sorting cells magnetically is an attractive approach for organizing or separating cells with anticipated properties from a heterogeneous population.^[53–55] For that aim, cells containing magnetic nanoparticles can be manipulated if the force exerted by the magnetic field gradient can overcome the hydrodynamic resistive forces the cells undergo in the fluid they are dispersed in or the inertia if deposited on a substrate.^[53] Accordingly, controlled separation of cells was attained employing the PS@IONPs microbeads previously internalized, with the cells detached from the substrate by trypsin treatment and upon exposure to a magnetic field gradient. The motion of these cells was analyzed by optical tracking and the mobilities evaluated taking into account mean-square displacements (MSD),^[56,57] in the absence and presence of the magnet field gradient and having the motion

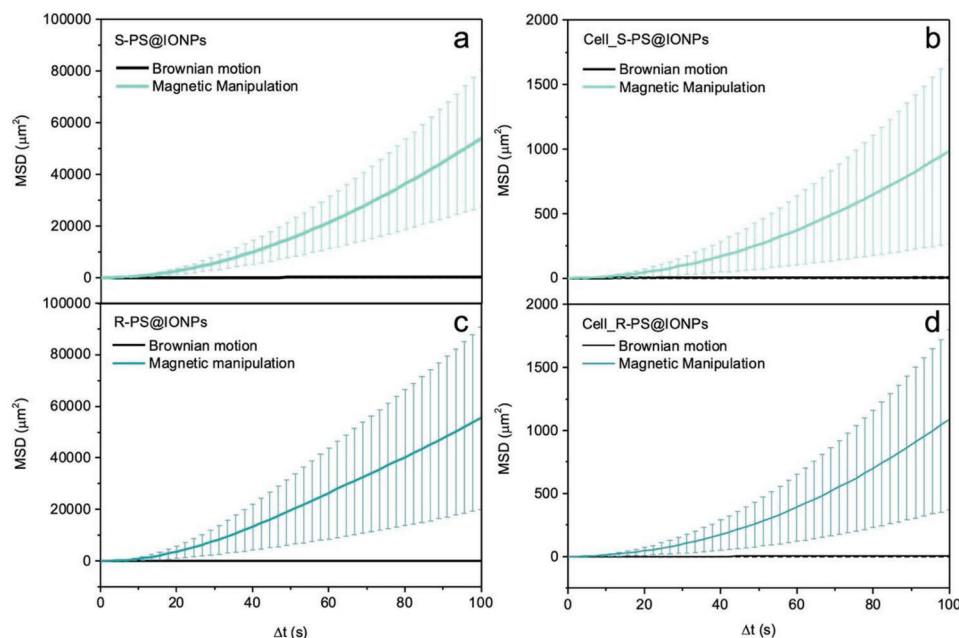


Figure 6. Mean squared displacements (MSD) plots with error bars representing standard deviations acquired from the a) S-PS@IONPs or c) R-PS@IONPs microbeads and of the A431 cells that have internalized the b) S-PS@IONPs or d) R-PS@IONPs microbeads, exhibiting diffusive (black linear curves) and ballistic (green parabolic curves) regimes when in the absence or presence of the magnetic field gradient, respectively.

of the microbeads in solution as reference. **Figure 6** shows these MSD plots associated to the motion of both the S-PS@IONPs and R-PS@IONPs microbeads (left column) and to the cells that have internalized them (right column), in the absence (black line-linear trend) and presence (green line-parabolic trend) of the magnetic field gradient, and for a rather long time interval.^[57] This is due to the low temporal resolution of the camera used, but since no dynamics occurring on a finer time scale will be considered, we proceeded with the interpretation of the data. Figure S9 (Supporting Information) includes a summary of subtracted trajectories of the S-PS@IONPs or R-PS@IONPs microbeads (a–d) and of the cells that have internalized them (e–h), without magnetic actuation (left column) or when under the influence of the magnetic field gradient (right column). As expected, both the microbeads and the cells move in random motion (Brownian) or show a magnetically guided movement (with linear trajectories toward the magnet because of the magnetic force exerted) under the conditions detailed, respectively. To evaluate these motions,^[55–57] the MSD plots were fitted, so as to calculate dynamic parameters such as the diffusion coefficient associated to the Brownian motion and the velocity in the case of directed motion. Diffusion coefficient values of 0.30 and 0.17 $\mu\text{m}^2 \text{s}^{-1}$ for the S-PS@IONPs or R-PS@IONPs microbeads, respectively, were calculated from the black linear plots shown in Figure 6a,c. The lower diffusion coefficient obtained for the R-PS@IONPs microbeads can be associated to the larger hydrodynamic radius, because of the electrostatic double layer and stability attained (reflected in a slightly larger value of ζ -potential when dispersed in water solution), because of the different surface topology. When considering the cells in solution, because of the much larger size of the object in motion and independently of the type of microbeads in their interior, the resulting diffusion

coefficients are $\approx 0.01\text{--}0.02 \mu\text{m}^2 \text{s}^{-1}$, meaning that they move very slowly in solution, as reflected by the extracted trajectories plotted in Figure S9e,g (Supporting Information).

When considering the guided movement and attending to the MSD parabolic functions displayed in Figure 6a,c, it is possible to check the similar response of the two types of microbeads when under the influence of the magnetic field gradient, stemming from the similar values of saturation magnetization [8.05 $\text{A m}^2 \text{kg}^{-1}$ (S-PS@IONPs) vs 8.14 $\text{A m}^2 \text{kg}^{-1}$ (R-PS@IONPs) at 300 K], and consequently similar magnetic force (acceleration) exerted on them. Nevertheless, the S-PS@IONPs became pulled faster, reaching a $2.38 \pm 0.21 \mu\text{m s}^{-1}$ velocity, compared to the $1.55 \pm 0.24 \mu\text{m s}^{-1}$ velocity of the R-PS@IONPs microbeads, likely due to the larger hydrodynamic radius of the later ones and therefore smaller magnetophoretic mobility (see the brief analysis of this parameter in the Supporting Information). However, when checking the movement induced to the cells (Figure 6b,d), though clearly showing a magnetically guided movement, there is no such big difference in the velocities reached by the magnetically manipulated cells which have internalized S-PS@IONPs ($0.31 \pm 0.04 \mu\text{m s}^{-1}$) or R-PS@IONPs ($0.28 \pm 0.03 \mu\text{m s}^{-1}$) microbeads. Naturally, for the similar magnetic field gradient, the cells ballistic motion induced was rather slow if compared to the microbeads alone, but still enough for an effective separation of cells.

As a matter of fact, the guided movement of the A431 cells when exposed to the magnetic field gradient, because having the magnetic microbeads internalized, was registered by time-lapse imaging (shown in Figure S10, Supporting Information). The time-lapse images of A431 cells labeled with S-PS@IONPs (left panel) and R-PS@IONPs (right panel) show their relative positions (indicated by the black vertical lines) every 140 s under

the influence of a magnetic field gradient (magnet located on the right of the images), dragged by the magnetic force exerted. Those cells without microbeads stay around a fixed position (indicated by the red vertical line). This demonstrates the effective magnetic manipulation of the A431 cells that have internalized the microbeads, rendering them cell translational vectors. This is actually key, for instance, in the delivery of cells or cellular materials, for the replacement and restoration of damaged tissue,^[58] though this kind of applications usually suffers from some limitations, such as poor targeting delivery or low therapeutic efficacy, due to low cell survival. In fact, the successful regeneration depends on the proliferation, survival and differentiation of transplanted cells at the exact locations following adequate delivery. With this into account, the cells that have internalized the microbeads when exposed to 100 $\mu\text{g}/\text{cell}$ culture and later isolated with the magnet, were allowed to grow overnight in a fresh medium. Images of the cell population, before and after magnet separation and growth overnight, were taken with confocal microscope in bright-field mode (included in Figure S11, Supporting Information), proving that the presence of these magnetic microbeads within the cells does not affect their viability, and preserves the normal proliferation. The A431 cells adhered and spread well on the plate surface, confirming that they are viable and can be grown successfully after the demonstrated spatial magnetic manipulation (see Videos S1 and S2, Supporting Information, of viable cells with internalized S-PS@IONPs or R-PS@IONPs microbeads, respectively, after magnetic cell sorting and grown overnight).

3. Conclusion

In summary, we fabricated PS@IONPs microbeads with different nanoscale surface topography and investigated its role in the cell uptake and intracellular fate. We found that the rougher topography given by elongated nanoparticles assists for an increase internalization of microbeads by A431 cells in the two routes considered: magnetic actuation and adsorptive uptake. However, the routes themselves determined the intracellular fate, leading the microbeads to end up free in the cytoplasm when using the magnetic actuation, or colocalized within late endosomes and lysosomes, in the case of the adsorptive uptake, independently of the nanoscale surface topography. We showed that cells bearing internalized microbeads can be spatially manipulated by applying a magnetic field gradient yielding good levels of substrate attachment, viability and growth. All things considered, this work highlights the nanoscale surface topography and the magnetic actuation potential, particularly in cell separation and cell delivery applications.

4. Experimental Section

Materials: Iron (III) chloride hexahydrate ($\text{FeCl}_3 \cdot 6\text{H}_2\text{O}$, $\geq 99\%$), iron (II) sulfate heptahydrate ($\text{FeSO}_4 \cdot 7\text{H}_2\text{O}$, 99%), hydrazine hydrate (N_2H_4 , 64%), sodium chloride (NaCl , 99%), hydrochloric acid (HCl , 37 wt%), ammonium hydroxide (NH_4OH , 28–30 wt%), tetramethylammonium hydroxide (TMAOH, 30 vol%), polyallylamine hydrochloride MW $\approx 17\,500$ (PAH), poly(sodium 4-styrene sulfonate) MW $\approx 70\,000$ (PSS), poly(fluorescein isothiocyanate allylamine hydrochloride) (PAH-FITC), phosphate-buffered solution (PBS, 10 \times), and ethanol anhydrous were

purchased from Sigma-Aldrich. Opti-MEM (1 \times) was supplied by Gibco, Thermo Fischer Scientific. Polystyrene spheres (PS, 1400 nm, 100 mL^{-1}) were purchased from Thermo Fischer Scientific, μ -Slides VI 0.4 were purchased from Ibsidi GmbH (Germany), Precision Plus Protein Dual-color standards (1610374), and Oriole fluorescent gel stain solution (1 \times) were purchased from BIO-RAD in Germany, Dulbecco's modified Eagle's medium (DMEM)-high glucose (Thermofisher, 11965092), Opti-MEM reduced serum medium (Thermofisher, 31985070), fetal bovine serum (FBS) (Sigma, F7524), penicillin-streptomycin (Thermofisher, 15070063), trypsin-EDTA solution (Merck, 59417C), formalin solution 10% neutral buffered (Sigma, HT501640). The following reagents were used for labeling subcellular components: LysoTracker Red DND-99 (Thermofisher, L7528), mouse anti-CD44 (GeneTex, GT981), rabbit anti-Rab 7 (Abcam, ab137029), goat anti-Rabbit IgG Alexa Fluor 594 (Thermofisher, A-11012), goat Anti-Mouse IgG Alexa Fluor 647 (Abcam, ab150115), and 4', 6-diamidino-2-phenylindole (DAPI) (Invitrogen, D1306). ProLong Gold Antifade Reagent (Thermofisher, P36930) were used as mounting medium for confocal microscopy. Cell proliferation studies were performed with 3-(4,5-dimethylthiazol-2-yl)-2,5-diphenyl tetrazolium bromide (MTT) Assay Kit (Abcam, ab211091) and Oriole Fluorescent Gel Stain (BioRad 1610496). Milli-Q water (18.2 $\text{M}\Omega \text{ cm}^{-1}$ resistance) was used in all aqueous preparations and washes.

Microbeads of PS Spheres Coated with Spherical Iron Oxide Nanoparticles (S-PS@IONPs): The synthesis of spherical iron oxide ($\text{Fe}_3\text{O}_4/\gamma\text{-Fe}_2\text{O}_3$) nanoparticles (IONPs) proceeded using the Massart's method.^[25] Accordingly, preprepared aqueous solutions of $\text{FeSO}_4 \cdot 7\text{H}_2\text{O}$ (1 mL, 2 M, in HCl 2 M) and $\text{FeCl}_3 \cdot 6\text{H}_2\text{O}$ (4 mL, 1 M) were simultaneously poured into 50 mL of NH_4OH solution (0.34 M) under mechanical stirring (650 rpm). After 30 min of mixing, the particles were allowed to settle. Following the separation of black sediment by a magnet, the obtained nanoparticles were washed with Milli-Q water several times and finally two times with TMAOH aqueous solution (0.1 M). At the final step, the particles were centrifuged (6000 rpm for 5 min) and redispersed in 50 mL of TMAOH aqueous solution via ultrasonication, to increase the surface charge and attain a better colloidal stability.

Subsequently, these as-synthesized IONPs were deposited onto PS spheres following the layer-by-layer (LbL) polyelectrolyte assembling.^[23] Thus, 25 μL of PS beads (100 mg mL^{-1} , 1.37 μm average diameter) were dispersed in 10 mL of positive polyelectrolyte (PAH, 2 mg mL^{-1}) aqueous solution (containing 0.5 M NaCl) and stirred for 30 min. Once the PS beads were centrifuged and washed with Milli-Q water, the same procedure was repeated using the negative polyelectrolyte (PSS, 2 mg mL^{-1}). Finally, 1 mg of the IONPs (stabilized with TMAOH, $\zeta = +33.8 \pm 1.0$ mV) aqueous solution was added to the polyelectrolyte coated PS spheres (PS@PAH/PSS) aqueous solution and stirred overnight (the final pH is kept at 7–8 to favor the electrostatic interactions between the nanoparticles and the polyelectrolyte). Subsequently, unbound nanoparticles were removed with several washes. For fluorescent labeling, 1 mg of the resultant PS@IONPs microbeads were dispersed in 0.5 mg of PAH-FITC solution [10 mL of NaCl aqueous solution (0.5 M)] and the reaction mixture was stirred overnight in dark. The resultant fluorescent microbeads of PS spheres coated with spherical IONPs and relatively smooth surface topography (S-PS@IONPs) were separated by centrifugation and washed with water.

Microbeads of PS Spheres Coated with Elongated Iron Oxide Nanoparticles (R-PS@IONPs): Magnetic microbeads with a rough surface topography were obtained following a two-step process by which first, elongated shaped akaganeite ($\beta\text{-FeOOH}$) nanoparticles were grown on the PS spheres and second, the $\beta\text{-FeOOH}$ antiferromagnetic phase is partially reduced to obtain a mixed iron oxide ($\text{Fe}_3\text{O}_4/\beta\text{-FeOOH}$) magnetic phase, such that microbeads of PS spheres coated with elongated IONPs and rougher surface topography (R-PS@IONPs) were produced. Accordingly, 0.1 M ferric chloride salt was homogeneously dispersed in 10 mL of aqueous PS bead solution (10 mg, 1.37 μm average diameter), and then the solution was placed in an oven at 60 $^\circ\text{C}$ to perform the hydrothermal growth for 6 h. At the end of the process, the particles were cooled to room temperature, collected by centrifugation (6000 rpm for 20 min), and washed several times with Milli-Q water. Subsequently, the $\beta\text{-FeOOH}$ spin-

dles formed on the surface of the PS spheres were treated with hydrazine, to induce the partial reduction of the β -FeOOH to Fe_3O_4 . Thus, 10 mg of as-synthesized PS@ β -FeOOH spiky nanostructures were dispersed in 15 mL of hydrazine aqueous solution (1:1 v/v). The solution was kept in preheated oven (120 °C) for 18 h. The resultant microbeads of PS spheres coated with elongated IONPs ($\text{Fe}_3\text{O}_4/\beta$ -FeOOH) and a rougher surface topography (R-PS@IONPs) were separated by centrifugation and washed with Milli-Q water.

Cellular Uptake, Staining, and Confocal Laser Scanning Microscopy (CLSM) Imaging: A431 cells (human epidermoid carcinoma cell line, ATCC, CRL-1555) were grown in DMEM-high glucose supplemented with 10% FBS, penicillin (10 000 units)-streptomycin (10 mg mL⁻¹) at 37 °C in a 5% CO₂ humidified atmosphere. When a sufficient number of cells was reached (1×10^5 cells were initially plated and grown to 60% confluence in 75 cm² flasks), the cells were detached by trypsin-EDTA solution and seeded onto sterile coverslips in a 24-well plate. After incubation overnight, the culture medium was removed, the cells were rinsed with Opti-MEM, and 100 μ L of magnetic microbeads (0.1 mg mL⁻¹) of each type were to the cells in 0.5 mL of Opti-MEM. The wells containing both the cells and the microbeads were placed under the influence of a magnetic field gradient for 15 min, to favor a magnetically induced cellular uptake, or just left overnight without the influence of the magnetic field gradient. Subsequently, cells were washed with Opti-MEM to remove the non-uptaken microbeads.

Lysosomal and cell membrane staining was performed as follows: Cells grown on coverslips were washed with PBS and incubated with 1 μ L Lyso-tracker in 1 mL of DMEM 10% FBS for 2 h at 37 °C. Next, the cells were incubated in blocking buffer: 10% (v/v) goat serum in PBS containing 0.05% (v/v) Tween 20. Staining of the cell membrane was performed with mouse-anti-human-CD44 (1:100) and goat anti-Mouse IgG Alexa Fluor 647 antibodies (1:500) in blocking buffer.^[35] Coverslips were rinsed with PBS and cells were fixed with formalin for 30 min. The cell nuclei were stained with DAPI and coverslips were mounted with ProLong on glass slides for CLSM.

Endosomal and cell membrane staining was performed as follows: Cells grown on coverslips were washed with PBS and fixed with formalin. The cells were then permeabilized with 0.1% (v/v) Triton X-100 in PBS, rinsed with PBS and incubated with blocking solution. Next, they were incubated with mouse-anti-human-CD44 (1:100) and rabbit-anti-human-Rab7 (1:100) antibodies in blocking solution, rinsed with PBS and incubated with goat anti-Rabbit IgG Alexa Fluor 594 (1:500) and goat anti-Mouse IgG Alexa Fluor 647 (1:500) antibodies in blocking solution. Cell nuclei were stained with DAPI and coverslips were mounted with ProLong on glass slides for CLSM.

Cell Lysis and SDS-PAGE Protein Analysis: To recover the magnetic particles in A431 cells and to analyze the proteins adsorbed on the particle surface, the cells were lysed in 150×10^{-3} M NaCl, 1% Triton 100x (NP-40), 50×10^{-3} M Tris buffer (pH 8) on ice and the particles were recovered by an external magnet. The particles were washed several times with PBS and dispersed in Laemmli Loading Buffer for SDS-PAGE analysis. The proteins were stained with Oriole Fluorescent gel staining solution.

Cytotoxicity Assays: The cytotoxicity of the particles on cells was examined by a colorimetric assay using an MTT reagent. Cells were grown in the 96-well cell culture plate for 24 h. Then, particles of different concentrations (from 50 to 300 μ g) were added onto cells (for $\approx 0.24 \times 10^6$ cells per well) in the presence of a magnet. After particle uptake (15 min for magnetic actuation and overnight for endosomal uptake), cells were washed several times with PBS, treated with 100 μ L of MTT reagent in Opti-MEM, and incubated in an oven at 37 °C for 3 h. At the end of the incubation, 150 μ L of MTT solvent was added for another 15 min incubation and the absorbance of solubilized formazan product was quantified at OD590 by EnVision Multimode Plate Reader. All experiments were performed three times and in triplicates.

Magnetic Manipulation of Microbeads and Cells Containing the Microbeads: To study the manipulation of the microbeads themselves or the cells containing the magnetic microbeads, under the influence of a magnetic field gradient, the microbeads were redispersed in water and placed on ibidi slides and the cells were first detached with trypsin-EDTA, redispersed in Opti-MEM and placed on ibidi slides. Time-lapse images were

recorded using a bright field microscope with a 20x objective (NIKON E800). The movies were recorded at 16 frames per second (fps) for 201 frames in the absence and presence of the magnetic field gradient. The trajectories of cells were tracked using the Fiji plugin TrackMate, extracted, and imported into Matlab for mean-square displacement analysis.^[56,57] Finally, cells that contain the magnetic microbeads were separated from the microbead-free cells using a magnet and transferred to a new flask. The readhesion and viability of the separated cells were monitored using an optical microscope (NIKON E800).

Statistical Analysis: One-way analysis of variance (ANOVA) by Tukey post hoc test to statistically compare among more than two different groups, and an independent and paired samples t-test for comparing between two groups were applied using SPSS. Statistical significance was assigned at a *p*-value of <0.05.

Characterization: TEM images were acquired to analyze the morphologies of obtained particles using a JEOL JEM 1010 device operating at 100 kV acceleration voltage. Size histograms were obtained by manually counting more than 200 particles using Fiji software. Layer-by-layer self-assembly was confirmed by ζ -potential measurements using a Malvern Zetasizer Nano series. Raman spectra were collected with a Renishaw in Via Reflex Confocal Raman Microscope. These experiments were registered in backscattering geometry at room temperature using a 785 nm laser excitation wavelength. The laser beam was focused on the sample by a 50x objective, and the laser power used 0.357 mW to avoid overheating or any transformations of the samples. X-ray diffraction (XRD) analysis was performed to determine the crystallographic structure of particles. XRD patterns were collected from powdered samples with a Panalytical X'Pert Pro diffractometer using Cu K α radiation (Bragg-Brentano θ - 2θ geometry) in the 2θ angular range of 10°–80° and a continuous scan mode (step = 0.02°, 4 s/step). Magnetic measurements of microbeads were performed using a vibrating sample magnetometer (VSM) option in a Physical Property Measurement System (PPMS) from Quantum Design. Hysteresis loops (*M*-*H* curves) were measured at 10 and 300 K applying an external magnetic field up to 5 T. The temperature-dependent magnetization in zero-field-cooling (ZFC) and field-cooling (FC) conditions was recorded applying a 10 mT magnetic field in a temperature range between 10 and 300 K. Dried powdered samples were used for all magnetic measurements. ICP-OES analysis was performed through Fe content analysis to quantify the intracellular uptake of particles for a known number of cells. Thus, magnetic particles including cells were detached by trypsinization, centrifuged, and finally, the cell-particle pellets were dissolved in 1 mL of HCl (37%)/H₂O solution (1:1 v/v) at 70 °C for 1 h. The analysis was performed in triplicate with percent error determined by calculating the standard deviation of these measurements. Fluorescence microscope images were obtained using a Nikon Ni-E direct microscope with a 100x objective. Images were taken with bright field and emission filters FTIC (excitation: 475/35 nm; emission: 530/43 nm; dichroic: 499). CLSM imaging was performed using Confocal Leica Microsystem (Stellaris 8) with the HC-PLAPO-CS2-40x/1.30-OIL, the HC-PLAPO-CS2-63x/1.40-OIL, or the HC-PLAPO-CS2-100x/1.40-OIL objectives. Images were acquired with Leica Application Suite X (LASX), software (Leica) in x-y-z scan mode, binning 512 \times 512, scan velocity 400 Hz (z-stacks 0.3 mm). A bright-field microscope with a camera (NIKON E800) was used for all magnetic manipulation experiments. EnVision Multimode Plate Reader (Perkin Elmer) was used to quantify absorbance values at OD590 for the MTT cytotoxicity assay.

Supporting Information

Supporting Information is available from the Wiley Online Library or from the author.

Acknowledgements

G.B. acknowledges financial support from the Xunta de Galicia (Centro singular de investigación de Galicia accreditation 2019–2022), from the

Spanish Ministerio de Ciencia e Innovación under Project No. PID2019-109669-RB-I00 and the European Union (European Regional Development Fund – ERDF). V.S. acknowledges the financial support by the Spanish Ministerio de Ciencia e Innovación under Project No. PID2020-119242-I00, and by the European Union Horizon 2020 Research and Innovation Program under the H2020 Marie Skłodowska-Curie Actions, Grant No. 872233 (“PEPSA-MATE”). Funding for open access by the Universidade de Vigo/CISUG.

Conflict of Interest

The authors declare no conflict of interest.

Data Availability Statement

The data that support the findings of this study are available from the corresponding author upon reasonable request.

Keywords

adsorptive uptake, magnetic manipulation, microbeads, surface topography

Received: May 4, 2023

Revised: August 28, 2023

Published online: September 21, 2023

- [1] Z. Ma, J. Mohapatra, K. Wei, J. P. Liu, S. Sun, *Chem. Rev.* **2023**, *123*, 3904.
- [2] Y. Chen, S. Hou, *Stem Cell Res. Ther.* **2022**, *13*, 135.
- [3] D. Chang, M. Lim, J. A. C. M. Goos, R. Qiao, Y. Y. Ng, F. M. Mansfeld, M. Jackson, T. P. Davis, M. Kavallaris, *Front. Pharmacol.* **2018**, *9*, 831.
- [4] A. Jordan, R. Scholz, K. Maier-Hauff, M. Johannsen, P. Wust, J. Nadobny, H. Schirra, H. Schmidt, S. Deger, S. Loening, W. Lanksch, R. Felix, *J. Magn. Magn. Mater.* **2001**, *225*, 118.
- [5] P. M. Price, W. E. Mahmoud, A. A. Al-Ghamdi, L. M. Bronstein, *Front. Chem.* **2018**, *6*, 619.
- [6] S. Díez-Villares, M. A. Ramos-Docampo, A. da Silva-Candal, P. Hervella, A. J. Vázquez-Ríos, A. B. Dávila-Ibáñez, R. López-López, R. Iglesias-Rey, V. Salgueiriño, M. de la Fuente, *Adv. Healthcare Mater.* **2021**, *10*, 2101019.
- [7] N. Lee, D. Yoo, D. Ling, M. H. Cho, T. Hyeon, J. Cheon, *Chem. Rev.* **2015**, *115*, 10637.
- [8] J. Kolosnjaj-Tabi, L. Lartigue, Y. Javed, N. Luciani, T. Pellegrino, C. Wilhelm, D. Alloyeau, F. Gazeau, *Nano Today* **2016**, *11*, 280.
- [9] A. Van de Walle, J. Kolosnjaj-Tabi, Y. Lalatonne, C. Wilhelm, *Acc. Chem. Res.* **2020**, *53*, 2212.
- [10] Y. Niu, M. Yu, S. B. Hartono, J. Yang, H. Xu, H. Zhang, J. Zhang, J. Zou, A. Dexter, W. Gu, C. Yu, *Adv. Mater.* **2013**, *25*, 6233.
- [11] H. Y. Lou, W. Zhao, Y. Zeng, B. Cui, *Acc. Chem. Res.* **2018**, *51*, 1046.
- [12] S. G. Higgins, M. Becce, A. Belessiotis-Richards, H. Seong, J. E. Sero, M. M. Stevens, *Adv. Mater.* **2020**, *32*, 1903862.
- [13] M. Babi, R. Riesco, L. Boyer, A. Fatona, A. Accardo, L. Malaquin, J. Moran-Mirabal, *ACS Appl. Bio Mater.* **2021**, *4*, 8443.
- [14] L. Krishna, K. Dhamodaran, K. Jayadev, K. Chatterjee, R. Shetty, S. S. Khora, D. Das, *Stem Cell Res. Ther.* **2016**, *7*, 188.
- [15] S. Park, H. H. Park, K. Sun, Y. Gwon, M. Seong, S. Kim, T. E. Park, H. Hyun, Y. H. Choung, J. Kim, H. E. Jeong, *ACS Nano* **2019**, *13*, 11181.
- [16] P. Lavrador, V. M. Gaspar, J. F. Mano, *Adv. Healthcare Mater.* **2020**, *9*, 1901860.
- [17] C. S. Tai, K. C. Lan, E. Wang, F. E. Chan, M. T. Hsieh, C. W. Huang, S. L. Weng, P. C. Chen, W. L. Chen, *Nano Lett.* **2021**, *21*, 1400.
- [18] X. Li, L. H. Klausen, W. Zhang, Z. Jahed, C. T. Tsai, T. L. Li, B. Cui, *Nano Lett.* **2021**, *21*, 8518.
- [19] R. K. Singh, J. C. Knowles, H. W. Kim, *J. Tissue Eng* **2019**, *10*, 204173141987752.
- [20] S. E. A. Gratton, P. A. Ropp, P. D. Pohlhaus, J. C. Luft, V. J. Madden, M. E. Napier, J. M. DeSimone, *Proc. Natl. Acad. Sci. USA* **2008**, *105*, 11613.
- [21] M. C. Debrosse, K. K. Comfort, E. A. Untener, D. A. Comfort, S. M. Hussain, *Mater. Sci. Eng., C* **2013**, *33*, 4094.
- [22] Y. F. Wang, Q. Zhang, F. Tian, H. Wang, Y. Wang, X. Ma, Q. Huang, M. Cai, Y. Ji, X. Wu, Y. Gan, Y. Yan, K. A. Dawson, S. Guo, J. Zhang, X. Shi, Y. Shan, X. J. Liang, *ACS Nano* **2022**, *16*, 4059.
- [23] F. Caruso, R. A. Caruso, H. Möhwald, *Science* **1998**, *282*, 1111.
- [24] V. Salgueiriño-Maceira, L. M. Liz-Marzán, M. Farle, *Langmuir* **2004**, *20*, 6946.
- [25] R. Massart, *IEEE Trans. Magn.* **1981**, *17*, 1247.
- [26] M. Testa-Anta, E. Tiryaki, L. Bocher, V. Salgueiriño, *Chem. Mater.* **2022**, *34*, 11026.
- [27] L. Yu, R. Han, X. Sang, J. Liu, M. P. Thomas, B. M. Hudak, A. Patel, K. Page, B. S. Guiton, *ACS Nano* **2018**, *12*, 9051.
- [28] M. Adhikari, E. Echeverria, G. Risica, D. N. McIlroy, M. Nippe, Y. Vasquez, *ACS Omega* **2020**, *5*, 22440.
- [29] M. Testa-Anta, M. A. Ramos-Docampo, M. Comesaña-Hermo, B. Rivas-Murias, V. Salgueiriño, *Nanoscale Adv.* **2019**, *1*, 2086.
- [30] M. Sanles-Sobrido, M. Bañobre-López, V. Salgueiriño, M. A. Correa-Duarte, B. Rodríguez-González, J. Rivas, L. M. Liz-Marzán, *J. Mater. Chem.* **2010**, *20*, 7360.
- [31] R. Otero-Lorenzo, E. Fantechi, C. Sangregorio, V. Salgueiriño, *Chem. - Eur. J.* **2016**, *22*, 6666.
- [32] E. Fröhlich, *Int. J. Nanomed.* **2012**, *7*, 5577.
- [33] A. B. Davila-Ibáñez, V. Salgueiriño, V. Martínez-Zorzano, R. Mariño-Fernández, A. García-Lorenzo, M. Maceira-Campos, M. Muñoz-Ubeda, E. Junquera, E. Aicart, J. Rivas, F. J. Rodríguez-Berrocá, J. L. Legido, *ACS Nano* **2012**, *6*, 747.
- [34] A. Vegerhof, E. A. Barnoy, M. Motiei, D. Malka, Y. Danan, Z. Zalevsky, R. Popovtzer, *Materials* **2016**, *9*, 943.
- [35] R. Di Corato, G. Béalle, J. Kolosnjaj-Tabi, A. Espinosa, O. Clement, A. K. A. Silva, C. Menager, C. Wilhelm, *ACS Nano* **2015**, *9*, 2904.
- [36] C.-H. Wu, Y.-Y. Huang, P. Chen, K. Hoshino, H. Liu, E. P. Frenkel, J. X. Zhang, K. V. Sokolov, *ACS Nano* **2013**, *7*, 8816.
- [37] G. Bodelón, V. Montes-García, C. Fernández-López, I. Pastoriza-Santos, J. Pérez-Juste, L. M. Liz-Marzán, *Small* **2015**, *11*, 4149.
- [38] A. Gautreau, K. Oguievetskaia, C. Ungermann, *Cold Spring Harbor Perspect. Biol.* **2014**, *6*, a016832.
- [39] C. Bucci, P. Thomsen, P. Nicoziani, J. McCarthy, B. Van Deurs, *Mol. Biol. Cell* **2000**, *11*, 467.
- [40] L. Langemeyer, F. Fröhlich, C. Ungermann, *Trends Cell Biol.* **2018**, *28*, 957.
- [41] B. Chazotte, *Cold Spring Harb. Protoc.* **2011**, pdb.prot5571.
- [42] A. Angelopoulou, A. Kolokithas-Ntoukas, C. Fytas, K. Avgoustakis, *ACS Omega* **2019**, *4*, 22214.
- [43] Z. Mao, X. Zhou, C. Gao, *Biomater. Sci.* **2013**, *1*, 896.
- [44] F. Lu, F. S.-H. Wu, Y. Hung, C. Y. Mou, *Small* **2009**, *5*, 1408.
- [45] M. Sousa De Almeida, E. Susnik, B. Drasler, P. Taladriz-Blanco, A. Petri-Fink, B. Rothen-Rutishauser, *Chem. Soc. Rev.* **2021**, *50*, 5397.
- [46] S. Zhang, H. Gao, G. Bao, *ACS Nano* **2015**, *9*, 8655.
- [47] Y. Portilla, V. Mulens-Arias, A. Paradela, A. Ramos-Fernández, S. Pérez-Yagüe, M. P. Morales, D. F. Barber, *Biomaterials* **2022**, *281*, 121365.

- [48] M. Testa-Anta, S. Liébaña-Viñas, B. Rivas-Murias, B. Rodríguez-González, M. Farle, V. Salgueiriño, *Nanoscale* **2018**, *10*, 20462.
- [49] J. Li, J. Wang, Q. Yao, T. Li, Y. Yan, Z. Li, J. Zhang, *Nanoscale* **2020**, *12*, 14911.
- [50] L. Zwi-Dantsis, B. Wang, C. Marijon, S. Zonetti, A. Ferrini, L. Massi, D. J. Stuckey, C. M. Terracciano, M. M. Stevens, *Adv. Mater.* **2020**, *32*, 1904598.
- [51] M. Bongaerts, K. Aizel, E. Secret, A. Jan, T. Nahar, F. Raudzus, S. Neumann, N. Telling, R. Heumann, J. M. Siaugue, C. Ménager, J. Fresnais, C. Villard, A. E. Haj, J. Piehler, M. A. Gates, M. Coppey, *Int. J. Mol. Sci.* **2020**, *21*, 6560.
- [52] Y. Kim, H. J. Jung, Y. Lee, S. Koo, R. Thangam, W. Y. Jang, S. Y. Kim, S. Park, S. Lee, G. Bae, K. D. Patel, Q. Wei, K. B. Lee, R. Paulmurugan, W. K. Jeong, T. Hyeon, D. Kim, H. Kang, *J. Am. Chem. Soc.* **2022**, *144*, 5769.
- [53] M. A. Ramos-Docampo, P. Hurtado, A. B. Dávila-Ibáñez, R. Piñeiro, M. L. Fanarraga, V. Salgueiriño, *J. Colloid Interface Sci.* **2023**, *629*, 287.
- [54] W. Tang, D. Jiang, Z. Li, L. Zhu, J. Shi, J. Yang, N. Xiang, *Electrophoresis* **2019**, *40*, 930.
- [55] H. Song, D. I. Kim, S. A. Abbasi, N. L. Gharamaleki, E. Kim, C. Jin, S. Kim, J. Hwang, J. Y. Kim, X. Z. Chen, B. J. Nelson, S. Pané, H. Choi, *Mater. Horiz.* **2022**, *9*, 3031.
- [56] G. Dunderdale, S. Ebbens, P. Fairclough, J. Howse, *Langmuir* **2012**, *28*, 10997.
- [57] W. Wang, T. E. Mallouk, *ACS Nano* **2021**, *15*, 15446.
- [58] X. L. Liu, S. Chen, H. Zhang, J. Zhou, H. M. Fan, X. J. Liang, *Adv. Mater.* **2019**, *31*, 1804922.